Design and Experimental Realization of a Broadband Transformation Media Field Rotator at Microwave Frequencies

Huanyang Chen, Bo Hou, Shuyu Chen, Xianyu Ao, Weijia Wen, and C. T. Chan*

Department of Physics, Hong Kong University of Science and Technology, Clear Water Bay, Kowlong, Hong Kong, China
(Received 24 January 2009; revised manuscript received 1 April 2009; published 8 May 2009)

We designed a metamaterial field rotator that can rotate electromagnetic wave fronts. Our starting point was the transformation-media concept. Effective medium theories and full simulations facilitated the actual design process. We created at a very simple structure comprising of an array of identical aluminum metal plates. We made and measured a sample and we experimentally demonstrated the field rotation effect as well as the broadband functionality at microwave frequencies.

PACS numbers: 42.25.Fx, 41.20.Jb, 42.25.Gy

Recently, the transformation-media concept has attracted the full attention of many researchers [1–26]. One reason for its popularity is its potential use in designs of invisibility cloaking devices [1–12]. Transformation media actually reaches beyond the ability to make things invisible. It can lead to many novel wave-manipulation devices, including field concentrators [13], field rotators [14,15], electromagnetic wormholes [16], impedance-matched hyperlenses [17], field shifters [18,19], anticloaks [20], cylindrical superlenses [21], superscatterers [22], superabsorbers [23], and remote cloaks [24]. Although the theory is flourishing, it is quite obvious that most real devices are very difficult to create in practice. It is useful to create devices for which real examples can be made and with which wave-manipulation functionality can be demonstrated experimentally. It is also desirable to create examples for which there are broadband functionalities, because the bandwidth issue is frequently identified as a major hurdle in the practical implementation of transformation-media devices. In this Letter, we describe an example with experimental evidence that demonstrates the functionality of a transformation-media based field rotator that operates at a wide bandwidth.

Based on the coordinate transformation methods [1,2], we proposed a two-dimensional transformation-media shell that can rotate fields but is itself invisible. The permittivity tensor and permeability of such a "field rotator" for transverse-electric (TE) polarized waves (whose magnetic field is in z direction) [14] are, respectively, described as

$$\overleftrightarrow{\varepsilon} = \begin{vmatrix} \varepsilon_{xx} & \varepsilon_{xy} \\ \varepsilon_{xy} & \varepsilon_{yy} \end{vmatrix}$$

and $\mu_z = 1$, where $\varepsilon_{xx} = \varepsilon_u \cos^2(\theta + \tau/2) + \varepsilon_v \sin^2(\theta + \tau/2)$, $\varepsilon_{xy} = (\varepsilon_u - \varepsilon_v)\sin(\theta + \tau/2)\cos(\theta + \tau/2)$, $\varepsilon_{yy} = \varepsilon_u \sin^2(\theta + \tau/2) + \varepsilon_v \cos^2(\theta + \tau/2)$, and $\varepsilon_u = (2 + t^2 - t\sqrt{t^2 + 4})/2$, $\varepsilon_v = (2 + t^2 + t\sqrt{t^2 + 4})/2$, $\cos\tau = \frac{t}{\sqrt{t^2+4}}$, $\sin\tau = \frac{2}{\sqrt{t^2+4}}$, where t is a constant. If these conditions are satisfied, the shell itself is invisible while it performs

the rotation. We note that for the ideal field rotator, ε_u and ε_v are related to τ. However, such a condition can be relaxed. As long as ε_u and ε_v are different (anisotropic), the metamaterial shell can still function as a rotator, but the shell itself will cause some scattering. We focus on this "reduced" field rotator due to its easy implementation.

We start from the specific pattern shown in Fig. 1 and use rectangular metal plates as building blocks to produce the anisotropic metamaterial. We first break up a concentric cylindrical shell whose dimensions are 12.5 mm < r < 50 mm into six concentric shells of equal thickness (6.25 mm). We divide each shell into cells each measuring 6.25 mm in the middle. Each cell has "fanlike" shape as shown in Fig. 1(b). From the inside to the outside, the number of cells in each ring increases from 16 to 22 to 28 to 34 to 41 to 47. A rectangular metal plate is placed in the
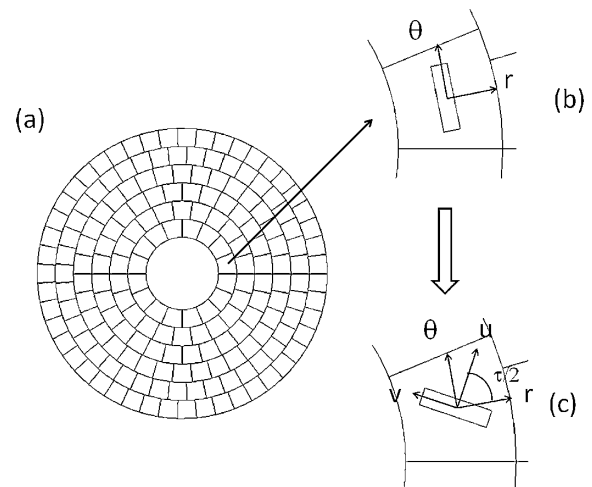

FIG. 1.   (a) A division of the field rotator into many cells with "fanlike" shapes with their principal axes in the r direction and the θ direction. (b) Each cell has a rectangular cylinder at its center with its longer side aligned with the tangential direction (the θ direction). (c) The field rotation effect can be achieved by rotating each rectangular cylinder around its center at a fixed angle $\tau/2$.

center of each cell so that the longer side is aligned with the tangential direction [the θ direction in Fig. 1(b)]. With a wavelength that is long compared with the metal plate dimensions, the metamaterial structure can be viewed as having concentric cylindrical shells with a position-dependent effective permittivity tensor, $\overleftrightarrow{\varepsilon} = \text{diag}\{\varepsilon_r, \varepsilon_\theta\}$, and permeability μ_z. This structure can also be viewed as a "zero-angle" field rotator, with parameters $\varepsilon_u = \varepsilon_r$, $\varepsilon_v = \varepsilon_\theta$, μ_z, and $\tau = 0$ (a zero rotation angle). We note that μ_z is less than unity [27]. The above metamaterial device can be used to produce a field rotation effect simply by rotating each rectangle anticlockwise around its center by $\tau/2$ [see Fig. 1(c)]. In the supplementary materials, we present the specific design with rectangles (4×1 mm^2) using the effective medium theory (EMT) [28]. The rotation angle depends on the anisotropy. The difference between ε_u and ε_v can be increased simply by using rectangles with larger aspect ratios. We use (6×1 mm^2) rectangles in the unit cell in the following section so that the rotation effect is stronger than the one in the supplementary materials. However, the EMT is not quantitatively accurate when the anisotropy is large, and in such situations, we have to employ brute-force full wave simulation for comparisons with experimental results. In the following, we set $\tau/2 = \pi/4$.

The experimental configurations are schematically shown in Fig. 2(a). The field rotator is a cylindrical object comprising 188 thin aluminum pieces arranged according to the theoretically designed pattern [see Fig. 2(b)]. We use a laser to cut the same pattern of slits with the same cross section in a thin slice of Plexiglas, and the Al pieces are inserted into these slits so that their relative positions can be fixed by the Plexiglas slice. By using several Plexiglas slices, we can fix the shape of the field rotator according to the theoretical blueprint, which has an annular cross section of 12.5 mm $< r <$ 50 mm and a length of 80 cm.

In the experiment, the samples are placed horizontally with the axis orientated along the z direction, and a horn-shaped antenna at a distance of $\sim$90 cm away from field rotator transmits microwaves toward the samples with the E field polarized along the vertical direction. To visualize the rotation effect of the electromagnetic field by the structure, we scan the spatial distribution of the H_z component across the field rotator by employing a split-ring antenna. The split-ring antenna has a circular loop with a diameter of 6 mm which has a 1 mm split at the front side of the loop, and the back side is broken and connected with the inner and outer conductors of a coaxial cable. The split-ring antenna as well as the coaxial cable is mounted on a two-dimensional translation stage and programmed to do point-by-point scanning in the vertical x-y plane. To scan the magnetic field inside the rotator, we cut the field rotator into two segments, each 40 cm long, and they are put next to each other with their axes aligned. A 5 mm air gap is maintained between the opposite cross sections of the two
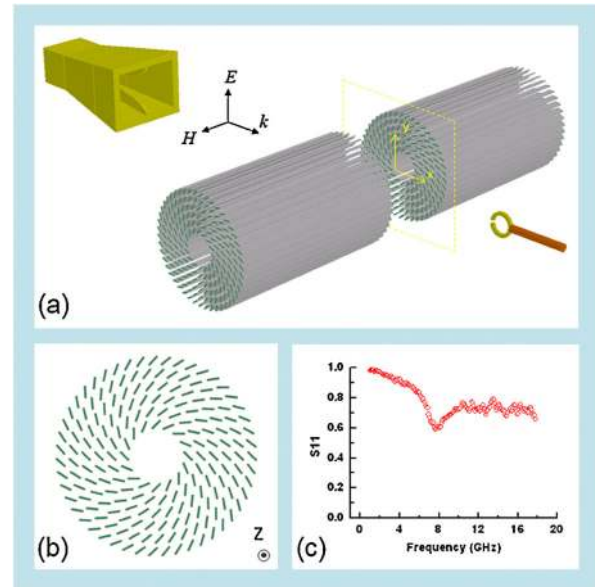

FIG. 2 (color online). (a) A schematic illustration of the samples (two segments of the field rotator) and the measurement setup, where the dashed lines mark the scanning region accessed by the split-ring antenna that is positioned by an automated stepping device. The dark green (dark gray) color on the cross sections of the samples is used to highlight the arrangement of Al pieces in the field rotator. The air gap between two segments of the field rotator has been exaggerated for visualization. (b) The arrangement pattern of the Al pieces viewed from the $+z$ direction. (c) The $S11$ response of the split-ring antenna.

segments to allow penetration of the split-ring antenna, as illustrated in Fig. 2(a). The scanning plane that is parallel to the two cross sections of the two segments of the field rotator is adjusted to pass through the air gap. The scanning area covers an area of 15×15 cm^2 with a spatial resolution of 2×2 mm^2, which is marked by the yellow (or light gray) dashed lines in Fig. 2(a). The ring plane of the detector antenna is set to be parallel to the x-y plane to probe the H_z component of the magnetic field. The horn-shaped antenna and the detector are connected to an S-parameter network analyzer to obtain the magnitude and phase spectra of the signal received by the detector [29]. The $S11$ parameter of the split-ring antenna is measured first and plotted in Fig. 2(c), which shows that magnetic resonance was found at 8.0 GHz. Accordingly, we set the sweep frequencies of the network analyzer to center on 8.0 GHz and we record the transmission magnitude and phase spectra, $A(x, y, f)$ and $\varphi(x, y, f)$ (where f is the frequency), respectively, at every spatial point (x, y) sampled by the split-ring antenna.

We utilize an 8.0 GHz TE polarized incident wave that is incident from left to right. The scattering patterns for an ideal and a reduced-field rotator are compared in Figs. 3(a) and 3(b). The inner radius is $r_1 = 12.5$ mm while the outer radius is $r_2 = 50$ mm. Figure 3(a) shows the scattering
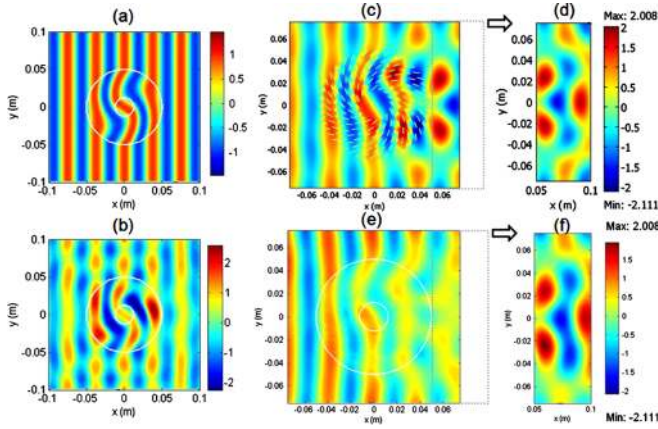
FIG. 3 (color online).   (a) The magnetic filed in the vicinity of
an ideal field rotator designed by transformation-media theory.
The results can be obtained analytically. (b) The magnetic field
in the vicinity of a reduced-field rotator (see text). It rotates the
field by the same angle as (a), but it causes some scattering.
(c) The simulated distribution of the H_z component propagating
from left to right across the field rotator at 8.0 GHz. In this field
rotator, the anisotropy is achieved by a collection of rectangular
metal plates. It can be viewed as a "discrete" version of the
reduced rotator. The shown region measures 15×15 cm^2,
where the axis unit is in meters. (d) The simulated distribution
of the H_z component immediately behind the field rotator ($x >$
50 mm) at 8.0 GHz. (e) The measured distribution of the H_z
component across the air gap depicted in Fig. 2(a) at 8.0 GHz.
The scanning region covers 15×15 cm^2, and the white circles
outline the interior and exterior boundaries of the field rotator.
(f) The measured distribution of the H_z component immediately
behind the middle part of a segment of the field rotator ($x >$
50 mm) at 8.0 GHz. Plots (c) and (d) share a color bar, and
plots (e) and (f) share a color bar.

pattern of a ideal field rotator with $\varepsilon_u = 0.5$, $\varepsilon_v = 2$, $\mu_z =$
1, and $\tau = \arccos(1/3)$. Figure 3(b) shows the scattering
pattern of a reduced-field rotator with $\varepsilon_u = 1.25$, $\varepsilon_v = 5$,
$\mu_z = 0.4$, and $\tau = \arccos(1/3)$. As discussed previously,
both can do field rotation, and the ideal rotator itself causes
no scattering while the reduced-field rotator causes some
scattering. Figures 3(c) and 3(d) show the simulated dis-
tribution of the H_z component propagating from left to
right across the structure at 8.0 GHz. Figure 3(e) shows the
corresponding experimental result of the distribution of H_z
at 8.0 GHz, measured as described above. We obtained the
real part of the measured quantity from the relation
$A(x, y, f) \cos[\varphi(x, y, f)]$ to compare the results with the
simulation. The white circles in Fig. 3(e) outline the inte-
rior and exterior boundaries of the field rotator, and the
slightly curved wave front of the incident plane wave is due
to the finite distance between the samples and the source
(the horn-shaped antenna). We see that at the center region
a $\sim 30°$ rotation of the electromagnetic wave occurs with
respect to the waves lying outside the field rotator. The
agreement with the simulation is very good, except for a

decrease in the intensity of the H_z component across the
field-rotator body with the x coordinate. This is caused by
the air gap in the measurement configuration, as mandated
by the experimental setup. An 8.0 GHz wave can only
tunnel through a 5 mm wide air gap (which has a cutoff
frequency of about 30 GHz to vertically polarized electro-
magnetic waves), which leads to a decrease in the intensity
of the electromagnetic field inside the field-rotator body as
well as behind the field rotator. We also ran a scan imme-
diately behind the middle part of a segment of the field
rotator far from the air gap [see Fig. 3(f)] and the result
behind the field rotator ($x > 50$ mm) shows full agreement
with the simulation [see Fig. 3(d)]. This agreement dem-
onstrates that the simulation can be trusted to a high degree
of confidence, and the experimental realization also faith-
fully produced the desired effect. The major reason for the
difference in the transmitted intensity between the mea-
sured and simulated field rotation is caused by the cutting
of the metamaterial cylinder into two segments for the
insertion of the automated step field sensor.

To study the bandwidth of the rotation effect, we also
used a small dipole antenna to detect the rotation effect
over a frequency band at three selected positions: $P1$
(5.8 cm in front of the field rotator), $P2$ (on the central
axis inside the field rotator), and $P3$ (2 cm behind the field
rotator), which are shown in Fig. 4(a). The 15 mm long
dipole antenna was positioned at these points and was
rotated in the x-y plane. The transmission magnitude spec-
tra were measured at different θ (denoting the angle be-
tween the dipole and the vertical direction) at these three
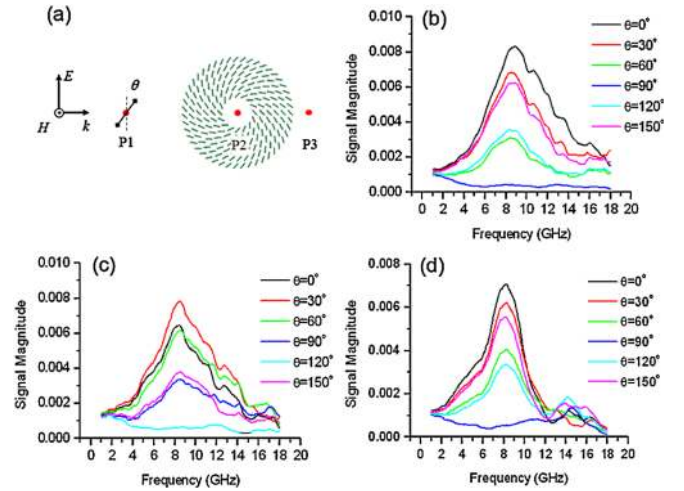positions. The results are presented in Figs. 4(b)–4(d). We

FIG. 4 (color online).   (a) A schematic of three selected posi-
tions to detect the rotation effect of the electromagnetic field.
The wave is incident from the left side. $P1$ is 5.8 cm in front of
the field rotator; $P2$ is on the central axis inside the field rotator;
and $P3$ is 2 cm behind the field rotator. θ indicates the angle
between the dipole (solid line) and the vertical direction (dashed
line). (b), (c) and (d) are the responses of the dipole antenna at
the three positions, $P1$, $P2$, and $P3$, respectively.

see that the signal magnitude is maximal at $\theta = 0°$ and minimal at $\theta = 90°$ both in front of and behind the field rotator [see Figs. 4(b) and 4(d)]. However, on the central axis inside the field rotator, the signal magnitude is maximal when $\theta = 30°$ and minimal when $\theta = 120°$ [see Fig. 4(c)], which verifies the 30° rotation of polarization inside the field rotator over a wide frequency band ranging from 2 to 10 GHz.

In conclusion, we have designed a field rotator using transformation optics. A reduced form of the rotator has a very simple geometry. We fabricated a rotator based on our design and its field rotation functionality was demonstrated in microwave experiments. We found rotation effect predicted theoretically in a broad frequency range.

---

*phchan@ust.hk

[1] U. Leonhardt, Science **312**, 1777 (2006).
[2] J. B. Pendry, D. Schurig, and D. R. Smith, Science **312**, 1780 (2006).
[3] D. Schurig, J. J. Mock, B. J. Justice, S. A. Cummer, J. B. Pendry, A. F. Starr, and D. R. Smith, Science **314**, 977 (2006).
[4] D. Schurig, J. B. Pendry, and D. R. Smith, Opt. Express **14**, 9794 (2006).
[5] W. Cai, U. K. Chettiar, A. V. Kildishev, and V. M. Shalaev, Nat. Photon. **1**, 224 (2007).
[6] H. Y. Chen, Z. Liang, P. Yao, X. Jiang, H. Ma, and C. T. Chan, Phys. Rev. B **76**, 241104(R) (2007).
[7] H. Chen, B.-I. Wu, B. Zhang, and J. A. Kong, Phys. Rev. Lett. **99**, 063903 (2007).
[8] Z. Ruan, M. Yan, C. W. Neff, and M. Qiu, Phys. Rev. Lett. **99**, 113903 (2007).
[9] W. Cai, U. K. Chettiar, A. V. Kildishev, V. M. Shalaev, and G. W. Milton, Appl. Phys. Lett. **91**, 111105 (2007).
[10] J. Li and J. B. Pendry, Phys. Rev. Lett. **101**, 203901 (2008).

[11] U. Leonhardt and T. Tyc, Science **323**, 110 (2009).
[12] R. Liu, C. Ji, J. J. Mock, J. Y. Chin, T. J. Cui, and D. R. Smith, Science **323**, 366 (2009).
[13] M. Rahm, D. Schurig, D. A. Roberts, S. A. Cummer, D. R. Smith, and J. B. Pendry, Photon. Nanostr. Fundam. Appl. **6**, 87 (2008).
[14] H. Y. Chen and C. T. Chan, Appl. Phys. Lett. **90**, 241105 (2007).
[15] Y. Luo, H. S. Chen, J. Zhang, L. Ran, and J. A. Kong, Phys. Rev. B **77**, 125127 (2008).
[16] A. Greenleaf, Y. Kurylev, M. Lassas, and G. Uhlmann, Phys. Rev. Lett. **99**, 183901 (2007).
[17] A. V. Kildishev and E. E. Narimanov, Opt. Lett. **32**, 3432 (2007).
[18] M. Rahm, S. A. Cummer, D. Schurig, J. B. Pendry, and D. R. Smith, Phys. Rev. Lett. **100**, 063903 (2008).
[19] H. Y. Chen and C. T. Chan, Phys. Rev. B **78**, 054204 (2008).
[20] H. Y. Chen, X. Luo, H. Ma, and C. T. Chan, Opt. Express **16**, 14 603 (2008).
[21] M. Yan, W. Yan, and M. Qiu, Phys. Rev. B **78**, 125113 (2008).
[22] T. Yang, H. Y. Chen, X. Luo, and H. Ma, Opt. Express **16**, 18545 (2008).
[23] J. Ng, H. Y. Chen, and C. T. Chan, Opt. Lett. **34**, 644 (2009).
[24] Y. Lai, H. Y. Chen, Z. Q. Zhang, and C. T. Chan, Phys. Rev. Lett. **102**, 093901 (2009).
[25] J. Yao, Z. Liu, Y. Liu, Y. Wang, C. Sun, G. Bartal, A. Stacy, and X. Zhang, Science **321**, 930 (2008).
[26] J. Valentine, S. Zhang, T. Zentgraf, E. Ulin-Avila, D. A. Genov, G. Bartal, and X. Zhang, Nature (London) **455**, 376 (2008).
[27] X. Hu, C. T. Chan, J. Zi, M. Li, and K.-M. Ho, Phys. Rev. Lett. **96**, 223901 (2006).
[28] See EPAPS Document No. E-PRLTAO-102-035921 for a specific design using the effective medium theory. For more information on EPAPS, see http://www.aip.org/pubservs/epaps.html. For the effective medium theory, see D. R. Smith, S. Schultz, P. Markos, and C. M. Soukoulis, Phys. Rev. B **65**, 195104 (2002).
[29] B. J. Justice, J. J. Mock, L. Guo, A. Degiron, D. Schurig, and D. R. Smith, Opt. Express **14**, 8694 (2006).